Spectral Characteristics of Fiber-Based S-Shape Taper Refractometer With High Sensitivity

Jianwen Ma, Haihao Cheng, Xuemei Yang, Songyang Zhang, Yongqi Li, Shun Wang, and Shun Wu

***Abstract*— In this work, we have experimentally demonstrated the refractive index (RI) sensing characteristics of a S-shape taper refractometer (STR) based on modal interference theory. Our preliminary theoretical analysis reveals that there exists a critical cladding mode, which is essential for understanding the sensing characteristics. When the dominant cladding mode involved in a core-cladding interference is close to the critical cladding mode, the resulting RI sensitivity tends to reach a maximum value. Moreover, both the critical and the dominant cladding mode are dependent on ambient RI. Our sensor achieves a high RI sensitivity of 2109.7 nm/RIU for a transmission dip at around 1505 nm with a measurement range of 1.36 to 1.39.**

***Index Terms*— Refractive index sensor, multimode interference, critical cladding mode.**

I. Introduction

REFRACTIVE index (RI) sensing measurement plays an important role in many application fields such as environmental safety monitoring [1], biochemical analysis [2], food safety [3] and etc. Among various configurations, fiber gratings [4], [5] and fiber-based modal interferometers [6]–[16] have attracted a growing interest due to their merits of high sensitivity combined with compact size and light weight. To date, many types of modal interferometers have been proposed and demonstrated: ranging from Fabry-Perot cavity [6], [7], Sagnac interferometers [8], [9], to Mach-Zehnder interferometers (MZI) [10]–[16]. Many kinds of techniques have been developed to fabricate MZIs such as fusion splice [10]–[14], femtosecond laser micromachining [15], [16], chemical etching [16], and etc., among which fiber tapering is a simple and effective way to realize high sensitivity. Tian *et. al.* reported the first tapered single-mode fiber MZI with a limited sensitivity of −17.1 nm/RIU [11]. Yang *et. al.* achieved a higher sensitivity of 1590 nm/RIU by fabricating a "S"-taper MZI via applying nonaxial pull in fiber tapering [12]. More recently, Li *et al.* reported a serial-tilted-tapered fiber for refractive index sensing. The sensitivity reaches 2300 nm/RIU, yet the structure is manufactural complex and fragile [13]. Our previous work demonstrates a refractive index sensor using a hollow-core silica tube sandwiched between two tapers, and achieving a sensitivity of −120.18 dB/RIU by demodulating the fringe contrast of the interference spectra [17]. In addition, an intensity demodulation method was utilized for spectral analysis of reflective refractometer based on S-tapered [18]. Despite they reported high sensitivity, the RI sensitivity characteristics of S-tapered fiber is less discussed.

In an S-tapered fiber, light propagating in the fiber core is excited to the cladding at the first bending. After travelling over a certain distance, the excited cladding modes are recoupled back into core at the second bending and interfere with the core mode. Thus, a typical Mach-Zehnder interferometer (MZI) is formed. Since the evanescent fields of various cladding modes extend differently to environment at the taper region, the RI sensitivity of the S-taper fiber sensor is cladding mode dependent. Reference [19] has analyzed the RI sensing characteristics of modal interferometers using SMF by introducing "sensitivity coefficient", which describes the response for a particular core- cladding mode interference dip to ambient refractive index (ARI). However, they did not experimentally study the underline principle between the RI sensitivity and the excited cladding mode for the S-taper fiber. In this work, we focus on studying how the tapering parameters influence the dominant excited cladding modes, and how the RI sensitivity is influenced by the modal interference.

In this letter, we present a theoretical analysis about the modal interference of fiber-based S-shape taper refractometer (STR). The theory indicates that there exists a critical cladding mode which determines the RI sensing characteristics for a core-cladding mode interference dip. When the involved cladding mode is close to the critical mode, for example, $HE_{1,10}$ in air, high sensitivity can be obtained. This agrees well with our experimental observation: a sensitivity of 2109.7 nm/RIU is realized for a transmission dip caused by the interference between the core mode and the $HE_{1,13}$ cladding mode. While other two STRs with $HE_{1,17}$ and $HE_{1,19}$ cladding modes involved exhibit lower sensitivity. This implies that the RI sensitivity can be enhanced by exciting cladding mode close to the critical mode. Furthermore, the behavior of the critical mode under different ARI is also studied.

II. Sensor Structure and Working Principle

In our experiment, a fusion splicer (Fujikura 80S) is utilized to fabricate STR using a standard SMF. We fabricated samples S1, S2 and S3 under the following splicer settings: tapering speed 25 bits, maximum vertical offset of 60 μm, and tapering length of 270 μm, 260 μm and 250 μm, respectively. The precise dimensions of each taper are measured and shown in the microscopic images in Fig. 1(a-c). Considering the taper

Manuscript received August 25, 2021; accepted September 18, 2021. Date of publication September 28, 2021; date of current version October 7, 2021. This work was supported by the National Natural Science Foundation of China under Grant 61805182 and Campus Grant 18QD19. *(Corresponding author: Shun Wu.)*

Jianwen Ma, Xuemei Yang, Songyang Zhang, Yongqi Li, Shun Wang, and Shun Wu are with Hubei Key Laboratory of Optical Information and Pattern Recognition, Wuhan Institute of Technology, Wuhan 430205, China (e-mail: wushun@wit.edu.cn).

Haihao Cheng is with the State Key Laboratory of Transient Optics and Photonics, Xi'an Institute of Optics and Precision Mechanics, Chinese Academy of Sciences, Xi'an 710119, China.

Color versions of one or more figures in this letter are available at https://doi.org/10.1109/LPT.2021.3115955.

Digital Object Identifier 10.1109/LPT.2021.3115955

1041-1135 © 2021 IEEE. Personal use is permitted, but republication/redistribution requires IEEE permission.
See https://www.ieee.org/publications/rights/index.html for more information.

Authorized licensed use limited to: Xi'an Institute of Optics and Precision Mechanics CAS. Downloaded on October 09,2021 at 02:20:46 UTC from IEEE Xplore. Restrictions apply.

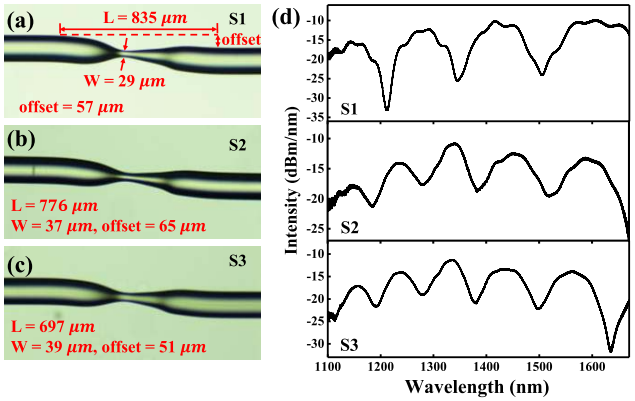

Fig. 1. Microscope images of (a) S1, (b) S2 and (c) S3. The measured dimensions of tapering length (L), vertical offset and waist (W) are shown. (d) Transmission spectra of S1, S2 and S3.

is a three-dimensional structure, we took multiple microscopic images with different axial rotation angles for each sample, and chose one with the longest tapering length. The tapering parameters were chosen such that the taper waist is small enough to form a strong evanescent field while maintaining good mechanical strength. The wavelength of a core-cladding interference dip can be expressed as [20]:

$$\lambda_{\mathrm{D}} = \frac{2\Delta n_{\mathrm{eff}} L_{\mathrm{eff}}}{(2\mathrm{m}+1)} \tag{1}$$

Here, $\Delta n_{\mathrm{eff}} = n_{\mathrm{co}}^{\mathrm{eff}} - n_{\mathrm{cl,m}}^{\mathrm{eff}}$ is the effective refractive index (ERI) difference between the core mode and m^{th}-order cladding mode. L_{eff} is the effective length for the dominant core-cladding interference. The samples were tested using a broadband laser source. Figure 1(d) shows the transmission spectra for S1, S2 and S3 in air. The insertion losses are around 10 dB. The spectra show regularly-spaced interference dips with small intensity modulations, indicating that a dominant interference pattern is formed with multiple weak interferences involved. The free spectral range (FSR) of the major interference is about 100-150 nm, which agrees with the value of Δn_{eff} between the core mode and low-order cladding mode. This implies that the pattern is mainly caused by core-cladding mode rather than cladding-cladding mode interference. Because Δn_{eff} of two adjacent cladding modes is nearly ten times smaller than that between the core and lower-order cladding mode, giving a FSR that would be at least hundreds of nm. Therefore, we will focus on the core-cladding mode interference involved in the following discussion.

In order to find out what cladding modes contribute to the interference, it is required to know the ERI of each mode. We calculated the ERI of the first fifteen cladding modes at 1550 nm by solving model eigenequations [21], as plotted in Fig. 2. The wavelength shift of resonance dip λ_{D} in response to ARI variation can be deduced from the Eqn. (1) [19],

$$\frac{d\lambda_{\mathrm{D}}}{dn_{\mathrm{am}}} = \chi \frac{\partial n_{\mathrm{cl,m}}^{\mathrm{eff}}}{\partial n_{\mathrm{am}}} \tag{2}$$

where

$$\chi = \frac{-\frac{\lambda_{\mathrm{D}}}{\Delta n_{\mathrm{eff}}}}{\left[1 - \frac{\lambda_{\mathrm{D}}}{\Delta n_{\mathrm{eff}}}\left(\frac{\partial n_{\mathrm{co}}^{\mathrm{eff}}}{\partial \lambda} - \frac{\partial n_{\mathrm{cl,m}}^{\mathrm{eff}}}{\partial \lambda}\right)\right]} \tag{3}$$

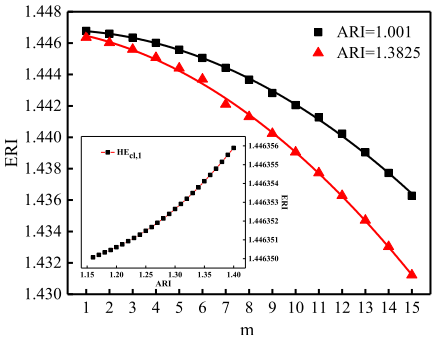

Fig. 2. The ERI of first fifteen cladding mode $HE_{1,m}$ at wavelength of 1550 nm, when ARI is 1.001 (black square) or 1.3825 (red triangle). The inset shows an ERI variation of first cladding mode $HE_{1,1}$ in ARI from 1.15 to 1.45.

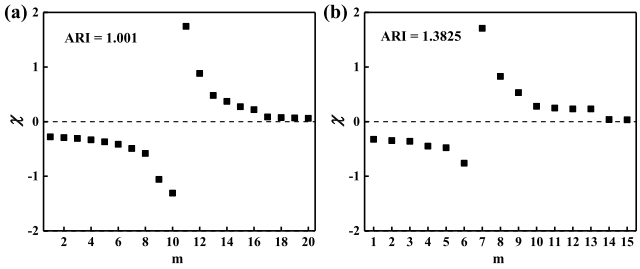

Fig. 3. The sensitivity coefficient χ of (a) first twenty $HE_{1,m}$ cladding modes when ARI = 1.001, (b) first fifteen $HE_{1,m}$ cladding modes when ARI = 1.3825.

is defined as the sensitivity coefficient of core-cladding mode interference. Subscript "co", "cl" and "am" denote for core, cladding and ambient, respectively. $\partial n_{\mathrm{cl,m}}^{\mathrm{eff}}/\partial n_{\mathrm{am}}$ is the partial differential term for the ERI with respect to the ARI variation. $\partial n_{\mathrm{co}}^{\mathrm{eff}}/\partial\lambda$ and $\partial n_{\mathrm{cl,m}}^{\mathrm{eff}}/\partial\lambda$ present the wavelength dependence of ERI for the core and m^{th}-order cladding mode, respectively. Figure 3 plots the sensitivity coefficient χ for first twenty $HE_{1,m}$ cladding modes in air and first fifteen $HE_{1,m}$ cladding modes in RI liquid (1.39) environment at wavelength of 1550 nm. In both cases, there exists a divergence point, defined as the "critical cladding mode". When in air, the order of the critical mode is between 10 and 11. However, when the ARI is 1.3825, it shifts to between 6 and 7. A possible explanation is as follows: the critical mode is the cladding mode when the coefficient χ flips sign, which is determined by the sign of the denominator of χ. The only term in the denominator affected by ARI is $\partial n_{\mathrm{cl,m}}^{\mathrm{eff}}/\partial\lambda$. When ARI increases, the ERI of cladding mode decreases faster as the order increases, resulting in a sign flip of χ.

To analyze the spatial frequency components in the transmission spectra, we performed fast Fourier transformation (FFT) for all three samples, as shown in Fig. 4(a). For S1, the dominant peak (solid black) appears at 0.0067 nm^{-1}, corresponding to a strong core-cladding interference. There are several weak frequency components, indicating multiple cladding modes involved. In our simulation, we only considered the core mode and two cladding modes. The optical path length values used are 855, 795, and 700μm for S1, S2 and S3, respectively, with the maximum deviation of 2.58% from the measured dimensions in Fig. 1(a-c). The resulting simulated spectra, represented by the blue curves, agree well with experimental results in Fig. 4(b-d). For S1, the dominant

Authorized licensed use limited to: Xi'an Institute of Optics and Precision Mechanics CAS. Downloaded on October 09,2021 at 02:20:46 UTC from IEEE Xplore. Restrictions apply.

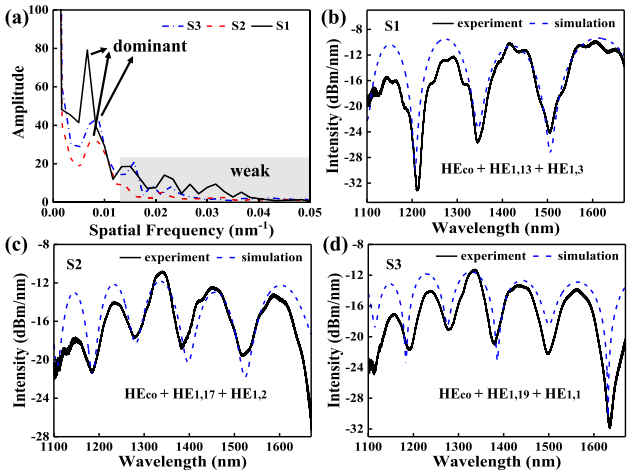

Fig. 4. (a) The spatial spectrum of S1, S2 and S3. The experimental (black line) and simulated (blue line) spectrum of (b) S1, (c) S2 and (d) S3 in air. The core mode HE_{co} and two cladding modes are considered in the simulation of (b-d).

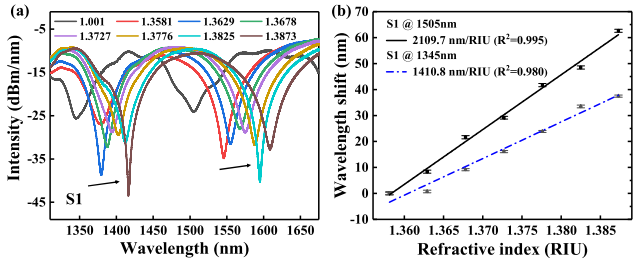

Fig. 5. (a) Transmission spectra of S1 at different ARI environment. (b) The wavelength shifts of resonant dip (1345 nm and 1505 nm) versus ARI.

cladding mode involved in the core-cladding interference is $HE_{1,13}$, interfering with core mode to form regularly-spaced dips in Fig. 4(b), while another weak mode $HE_{1,3}$ gives rise to the background intensity modulation. The dominant cladding modes are $HE_{1,17}$, $HE_{1,19}$ for S2, S3, respectively.

III. RI Sensing Performance and Discussions

In this section, the ARI responses of STRs were measured by immersing the sensing element in various RI liquids (Cargille index matching oil, Series AAA). All RI values used correspond to the measured wavelengths. The transmission spectra of S1 are plotted in Fig. 5(a). The interference dip around 1505nm shows an average sensitivity of 2109.7 nm/RIU, as shown in Fig. 5(b). This result is comparable to the result reported in Reference [20] (2066 nm/RIU) but with twice the measurement range. Considering S1 has less vertical offset, our sensor is expected to have better mechanical strength than Reference [19]. The results also show wavelength dependency for the RI sensitivity. At a shorter wavelength of 1345 nm, the sensitivity was measured to be 1410.8 nm/RIU. Error bars were added for all data points indicating a small wavelength uncertainty. For comparison, the RI responses of S2 and S3 are also recorded in Fig. 6. We employed binomial fitting for the wavelength shift. The sensitivity reaches maximum value of 1962.9 nm/RIU around 1498 nm for S2, and 1867.6 nm/RIU around 1518 nm for S3. According to the simulation, the dominant mode involved in interference for S2 and S3 are $HE_{1,17}$ and $HE_{1,19}$ in air. Similar sensitivity performances for both samples is expected

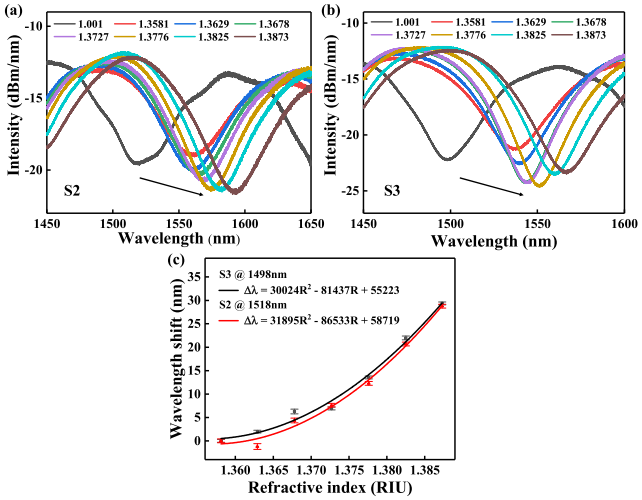

Fig. 6. Transmission spectra of (a) S2, and (b) S3 at different ARI environment. (c) The wavelength shifts of resonant dip (1498 nm for S3 and 1518 nm for S2) versus ARI.

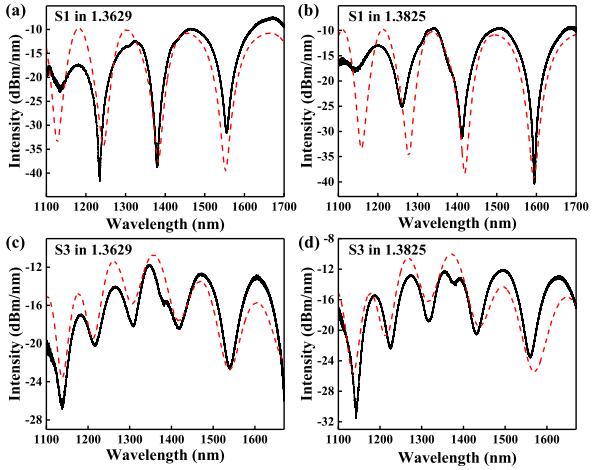

Fig. 7. Simulated spectra (red) of S1 in ARI of (a) 1.37, (b) 1.39, and S3 in ARI of (c) 1.37, (d) 1.39. Experimental spectra (black) are shown for comparison.

because the calculated sensitivity coefficients (Fig 3 (a)) for both cladding modes are comparable. The different RI response of S2, S3 compared to S1 is mainly due to the various interaction strength between the leaked evanescence waves and the environment. The taper waist in combination with the offset determines the excitement of high order cladding modes and the optical path length for the interference. The order of the dominant cladding mode is largely affected by the physical shape of the taper. For S-tapers with thinner waist with larger vertical offset, the evanescence waves have a stronger interaction with the environment, leading to a higher RI sensitivity [23]. However, this also results in larger insertion loss. One would have to balance between sensitivity and transmission loss for the sensor design.

To investigate the underline relationship between the dominant cladding mode with ambient RI, we further simulated the transmission spectra in different ARI. Figure 7 shows the simulated spectra for S1 and S3 in an ARI of 1.37 and 1.38, respectively. Figure 8 shows the dominant cladding modes in different ARIs from 1.001 to 1.39, illustrated as red dots for S1, green up-triangles for S2 and blue down-triangles for S3.

Authorized licensed use limited to: Xi'an Institute of Optics and Precision Mechanics CAS. Downloaded on October 09,2021 at 02:20:46 UTC from IEEE Xplore. Restrictions apply.

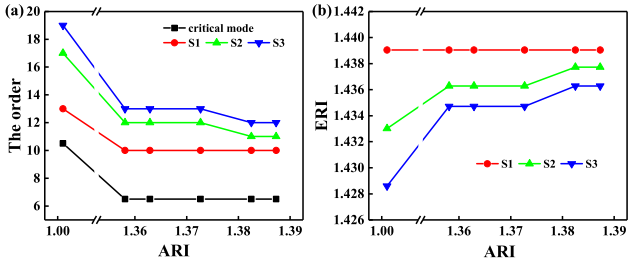

Fig. 8. When in different ambient RI (ARI), (a) The order of the critical mode, and three STR's dominant cladding modes, and (b) corresponding ERI variation of three STR's dominant cladding modes as a function of ARI.

We also plotted how the order of the critical mode varies with the ARI, shown in black squares. Among the three STRs, the dominant cladding mode for S1 is remains the closest to the critical mode for all ARIs, which explains why S1 has a higher sensitivity than S2 and S3. The common trend is that both the critical mode and the dominant cladding modes shift to lower orders as ambient environment changes from air to RI liquid. We can see that the dominant cladding mode of S1 remains to be $HE_{1,10}$ for different RI liquids, while that of S2 and S3 get closer to the critical mode as ARI rises from 1.37 to 1.38, indicating a rise in sensitivity for higher ARI. This can possibly explain why S1 shows linear wavelength shift (Fig. 5(b)) while the performance for S2 and S3 are nonlinear in higher ARI (Fig. 6(c)). Figure 8(b) shows the corresponding ERI of the dominant cladding modes as a function of the ARI.

It is worth noting that this preliminary simulation results certainly have limitations, for example, we only considered two cladding modes; we used wavelength at 1550nm, whereas broadband source is utilized in the experiment. However, our experimental results agree with the simulations to some extent. We believe this qualitative simulation gives insight for understanding modal interference behavior in tapered structures, and also offers an effective way of fabricating highly sensitive tapered fiber sensors based on modal interference.

IV. Conclusion

In summary, we experimentally demonstrated the RI sensitivity characteristic of STR. Our theory reveals that there exists a critical cladding mode to determine the sensing characteristics, in which the RI sensitivity tends to increase as the dominant cladding mode approaches the critical mode. These preliminary simulation findings are verified by our experimental results. The maximum sensitivity we obtained is 2109.7 nm/RIU at 1505 nm, which is from the interference between the core mode and $HE_{1,13}$ cladding mode. Our study shows that following the designing rule based on the critical mode theory, RI sensing sensitivity can be effectively improved, even for other similar types of MZIs [24]. Considering the mechanical strength of the sensor, it's expected to be used with open case packaging to allow liquid infiltration. The proposed sensor can be applied in biological and chemical sensing fields.

References

[1] L. J. Zu, H. M. Zhang, Y. P. Miao, B. Li, and J. Q. Yao, "Microfiber coupler with a Sagnac loop for water pollution detection," *Appl. Opt.*, vol. 58, no. 21, pp. 5859–5864, Jul. 2019.

[2] X. Zhang *et al.*, "Label-free detection of DNA hybridization utilizing dual S-tapered thin-core fiber interferometer," *J. Lightw. Technol.*, vol. 37, no. 11, pp. 2762–2767, Jun. 1, 2019.

[3] Y. Yin, S. Li, J. Ren, G. Farrell, E. Lewis, and P. Wang, "High-sensitivity salinity sensor based on optical microfiber coil resonator," *Opt. Exp.*, vol. 26, no. 26, pp. 34633–34640, Dec. 2018.

[4] Y. Zhang *et al.*, "Refractive index sensing based on higher-order mode reflection of a microfiber Bragg grating," *Opt. Exp.*, vol. 18, no. 25, pp. 26345–26350, 2010.

[5] T. Geng *et al.*, "A temperature-insensitive refractive index sensor based on no-core fiber embedded long period grating," *J. Lightw. Technol.*, vol. 35, no. 24, pp. 5391–5396, Dec. 15, 2017.

[6] J. J. Tian, Z. J. Lu, M. R. Quan, Y. Z. Jiao, and Y. Yao, "Fast response Fabry–Pérot interferometer microfluidic refractive index fiber sensor based on concave-core photonic crystal fiber," *Opt. Exp.*, vol. 24, no. 18, pp. 20132–20142, Sep. 2016.

[7] X. Yang *et al.*, "Simplified highly-sensitive gas pressure sensor based on harmonic Vernier effect," *Opt. Laser Technol.*, vol. 140, Aug. 2021, Art. no. 107007.

[8] J. Yuan *et al.*, "Reflective long-period fiber grating-based sensor with Sagnac fiber loop mirror for simultaneous measurement of refractive index and temperature," *Appl. Opt.*, vol. 53, no. 29, p. H85, Oct. 2014.

[9] S. Y. Xiao *et al.*, "Simultaneous measurement of refractive index and temperature using SMP in Sagnac loop," *Opt. Laser Technol.*, vol. 96, pp. 254–258, Nov. 2017.

[10] X. Yu, X. Chen, D. Bu, J. Zhang, and S. Liu, "In-fiber modal interferometer for simultaneous measurement of refractive index and temperature," *IEEE Photon. Technol. Lett.*, vol. 28, no. 2, pp. 189–192, Jan. 15, 2016.

[11] Z. Tian *et al.*, "Refractive index sensing with Mach–Zehnder interferometer based on concatenating two single-mode fiber tapers," *IEEE Photon. Technol. Lett.*, vol. 20, no. 8, pp. 626–628, Apr. 15, 2008.

[12] R. Yang, Y. S. Yu, Y. Xue, C. Chen, Q. D. Chen, and H. B. Sun, "Single S-tapered fiber Mach–Zehnder interferometers," *Opt. Lett.*, vol. 36, no. 23, pp. 4482–4484, Dec. 2011.

[13] Y. Li *et al.*, "Serial-tilted-tapered fiber with high sensitivity for low refractive index range," *Opt. Exp.*, vol. 26, no. 26, pp. 34776–34788, Dec. 2018.

[14] Q. Rong, X. Qiao, R. Wang, H. Sun, M. Hu, and Z. Feng, "High-sensitive fiber-optic refractometer based on a core-diameter-mismatch Mach–Zehnder interferometer," *IEEE Sensors J.*, vol. 12, no. 7, pp. 2501–2505, Jul. 2012.

[15] Y. F. Zhang, C. R. Liao, C. P. Lin, Y. Shao, Y. Wang, and Y. P. Wang, "Surface plasmon resonance refractive index sensor based on fiber-interface waveguide inscribed by femtosecond laser," *Opt. Lett.*, vol. 44, no. 10, pp. 2434–2437, May 2019.

[16] X.-Y. Sun *et al.*, "Highly sensitive refractive index fiber inline Mach–Zehnder interferometer fabricated by femtosecond laser micromachining and chemical etching," *Opt. Laser Technol.*, vol. 77, pp. 11–15, Mar. 2016.

[17] S. Wu, H. H. Cheng, J. W. Ma, X. M. Yang, S. Wang, and P. X. Lu, "Temperature-independent ultra-sensitive refractive index sensor based on hollow-core silica tubes and tapers," *Opt. Exp.*, vol. 29, no. 7, pp. 10939–10948, Mar. 2021.

[18] P. Niu, J. Zhao, C. Zhang, H. Bai, X. Sun, and J. Bai, "Reflective intensity-demodulated refractometer based on S fiber taper," *IEEE Photon. Technol. Lett.*, vol. 30, no. 1, pp. 55–58, Jan. 1, 2018.

[19] Y. Zhang *et al.*, "Refractive index sensing characteristics of single-mode fiber-based modal interferometers," *J. Lightw. Technol.*, vol. 32, no. 9, pp. 1734–1740, May 1, 2014.

[20] R. Yang *et al.*, "S-tapered fiber sensors for highly sensitive measurement of refractive index and axial strain," *J. Lightw. Technol.*, vol. 30, no. 19, pp. 3126–3132, Oct. 1, 2012.

[21] C. Tsao, D. Payne, and W. A. Gambling, "Modal characteristics of three-layered optical fiber waveguides: A modified approach," *J. Opt. Soc. Amer. A, Opt. Image Sci.*, vol. 6, no. 4, pp. 555–563, Apr. 1989.

[22] J. Yang, L. Yang, C. Q. Xu, and Y. Li, "Optimization of cladding-structure-modified long-period-grating refractive-index sensors," *J. Lightw. Technol.*, vol. 25, no. 1, pp. 372–380, Jan. 2007.

[23] C. Chen *et al.*, "Compact refractive index sensor based on an S-tapered fiber probe," *Opt. Mater. Exp.*, vol. 8, no. 4, pp. 919–925, 2018.

[24] J. Ma, S. Wu, H. Cheng, X. Yang, S. Wang, and P. Lu, "Sensitivity-enhanced temperature sensor based on encapsulated S-taper fiber modal interferometer," *Opt. Laser Technol.*, vol. 139, Jul. 2021, Art. no. 106933.

Authorized licensed use limited to: Xi'an Institute of Optics and Precision Mechanics CAS. Downloaded on October 09,2021 at 02:20:46 UTC from IEEE Xplore. Restrictions apply.